


# Light-induced ferromagnetic resonance shift in magnetoelectric heterostructure

Pankaj Pathak<sup>1,\*</sup>, Ajay Kumar<sup>2</sup>, and Dhiman Mallick<sup>1,†</sup>

<sup>1</sup>*Department of Electrical Engineering, Indian Institute of Technology Delhi, New Delhi 110016, India*

<sup>2</sup>*Department of Physics, Indian Institute of Technology Delhi, New Delhi 110016, India*

 (Received 26 June 2023; revised 18 August 2023; accepted 2 October 2023; published 20 October 2023)

The resonant control of the spin magnetic moment using ferromagnetic resonance (FMR) could enable an energy-efficient route for low-power spintronic devices for neuromorphic and signal processing applications. However, resonant spin control by FMR usually requires a rf magnetic field or high-density spin-polarized current resulting in high power consumption. Instigating FMR directly with an external electric field using magnetoelectric (ME) materials can offer an energy-efficient alternative due to large strain-mediated ME coupling. Yet, this method requires a high-saturation electric field that could cause device malfunction due to dielectric breakdown. Also, the necessity to make electrical contacts in ME materials leads to complexity. In this work, we demonstrate light-induced FMR tunability in Ni/PMN-PT ME heterostructure at room temperature. We show that light generates piezostain in PMN-PT without any bias voltage and controls the spin dynamics of the ferromagnetic Ni thin film. Depending on the direction of the external applied magnetic field with respect to the PMN-PT crystalline directions, upward and downward volatile FMR shift is demonstrated. We also show that FMR shift can be induced by increasing the irradiation time at constant illumination power. This technique presents a remote means to control the spin magnetic moment for next-generation light-controlled ME-based rf and microwave devices, allowing easier integration of these devices into complex architectures by eliminating the need for direct electrical contacts or bulky external components.

DOI: [10.1103/PhysRevApplied.20.044055](https://doi.org/10.1103/PhysRevApplied.20.044055)

## I. INTRODUCTION

Recently, coherent resonant control of the spin magnetic moment in nanoscale spintronic oscillators through magnetization precession has expedited the exploration of next-generation neuromorphic-based spintronic and signal processing devices [1,2]. In particular, researchers have explored the collective excitation of magnetic spins in the ferromagnetic layer of nanoscale spintronic oscillator using ferromagnetic resonance (FMR) for neuromorphic computing combined with tunable microwave frequency and CMOS compatibility [3–5]. To realize different neuromorphic functions, direct control of FMR is greatly desired. Indeed, nano-oscillator-based neuromorphic devices are lately implemented to recognize the signal pattern by controlling the spin dynamics in FMR of an individual oscillator [4].

Conventionally, the rf magnetic field is used to control the spin dynamics in FMR [2,4–8]. A transverse rf magnetic field is applied to excite the stable spin precessional dynamics under a static magnetic field so that the energy of the rf magnetic field is effectively absorbed. It is achieved

when the frequency of the rf magnetic field is tuned to the spin precessional frequency [3,6]. Usually, the external electric current that flows through the conductive coil is used to generate the requisite magnetic field. However, the fundamental problem of rf control is its disability to develop a highly localized magnetic field, especially at the nanometer-scale range [6]. Additionally, this arrangement turns the device noisy, bulky, and energy inefficient. This is a severe problem, especially when device size and power consumption are primary concerns. Later, spin-transfer torque (STT) is proposed to control the spin dynamics in FMR to overcome these problems [9–11]. However, this resulted in the incoherent control of the spin magnetic moments as the STT effect emerged from the decoherence spin angular moment [12]. Additionally, to observe the spin transfer effect, a high current density (approximately equal to  $10^{10}$  A/m<sup>2</sup>) is required resulting in high power consumption due to Joule heating [13,14]. Consequently, the device operation, especially for larger tunability is impractical.

Instigating FMR directly with an external electric field using magnetoelectric (ME) materials can offer an energy-efficient alternative due to large strain-mediated ME coupling [15–19]. ME materials consist of a ferromagnet (FM) and ferroelectric (FE) order parameter simultaneously

\*[pankaj.pathak@ee.iitd.ac.in](mailto:pankaj.pathak@ee.iitd.ac.in)

†[dhiman.mallick@ee.iitd.ac.in](mailto:dhiman.mallick@ee.iitd.ac.in)

[20–23]. In these materials, an external electric field is applied across the FE layer to generate the piezoelectric strain that instigates the effective magnetic anisotropy in the FM layer and subsequently controls the spin magnetic moment and magnetization in FMR. Therefore, electric field control is a faster, more energy efficient, and more coherent control method of the spin magnetic moment than its earlier counterparts. However, the primary obstruction in this method is the requirement of the high-saturation electric field (approximately equal to 1 MV/m) that could cause device malfunction due to dielectric breakdown [24,25]. Also, for practical applications, a high electric field could generate parasitic capacitance, which could act as a low-pass filter and hinder the device operation at high frequencies. Additionally, from a device point of view, the necessity to make electrical contacts in ME heterostructure leads to complexity as the dimension of ME-based microwave devices continues to shrink [26].

One promising avenue to overcome these limitations in ME heterostructure is the light-induced piezostain generation in the FE layer to control the spin dynamics of the FM layer. FEs generate piezostain under light illumination due to photon-electron interaction, as FEs are insulators with moderate band gap [27]. This approach holds promise for device miniaturization through the substitution of conventional voltage sources in ME heterostructure with optical alternatives. The miniaturization of rf and microwave devices offers substantial potential for practical applications, driving advancements in communication systems, sensing technologies, and wireless devices, as these devices not only demand reduced power consumption but are also imperative for device mass reduction [15–18]. Additionally, higher computational density could be achieved by incorporating such devices as nanoscale spintronic oscillators in neuromorphic-based spintronic and signal processing devices.

The light-induced piezostain in FEs is attributed to the photostriction or photocontraction effect [26–34]. When a FE material is irradiated with light of a specific intensity and wavelength, possessing energy greater than the band gap of the FE material, the material absorbs photons from the incident light [26–34]. This absorption process creates electron-hole ( $e-h$ ) pairs or charge carriers within the material due to band-to-band transition. These charge carriers are spatially separated within the material, leading to the modification of the internal electric field ( $E_i$ ) due to the bulk photovoltaic effect [28,29]. Since the polarization of a FE material results from the arrangement of positive and negative charges within its crystal lattice, the modified  $E_i$  changes the magnitude and orientation of the FE polarization. Consequently, this modified polarization gives rise to the generation of piezostain due to the inverse piezoelectric effect. Additionally, the interaction of incident photons with the FE material may result in localized heating, leading to a temperature rise attributed to the pyroelectric effect

[35–37]. The pyroelectric effect characterizes the intrinsic behavior of FE materials, wherein fluctuations in temperature induce alterations in the positions of constituent atoms within the crystal lattice due to the lattice vibrations. Consequently, these atomic displacements influence charge distributions within the material, further modulating its net polarization. This polarization adjustment corresponds to variations in the dipole moment of the FE material. Significant development of strain generation under light illumination by FEs was first reported by Tatzuzakiet *et al.* [28] in SbSI ferroelectric crystal. Kundys *et al.* [29] showed a substantial dimensional change of BiFeO<sub>3</sub> (BFO) crystal under light irradiation at room temperature. Hu *et al.* [30] successfully modulated ferroelectric tunnel junction memory states under light illumination using Sm-doped BFO ferroelectric layer. Makhort *et al.* [31] showed generation of saturation polarization in Pb[(Mg<sub>1/3</sub>Nb<sub>2/3</sub>)<sub>x</sub>Ti<sub>1-x</sub>]O<sub>3</sub> (PMN-32%PT) FE due to the photovoltaic effect under light irradiation. This drew researchers attention to light-induced magnetization excitation in the ME heterostructure also. Iurchuk *et al.* [32] showed light-controlled coercivity modulation of nickel (Ni) thin film in Ni/BFO (FM/FE) heterostructure. Zhang *et al.* [33] showed volatile 90° magnetization modulation of Ni thin film using Ni/PMN-PT (FM/FE) heterostructure under light irradiation to study magnetic memory and logic devices. Dagur *et al.* [34] showed light-induced effects in Ni/PMN-PT (FM/FE) heterostructure while confirming the necessity for spectroscopic techniques to elucidate the physical origin of interface behavior.

However, it is worthwhile to note that thus far, these studies have primarily focused on static magnetization control only, and light-induced dynamic magnetization control using FMR, which has significant practical relevance for realizing remote-tunable oscillators for neuromorphic and other spin-based applications, has been elusive. FMR has crucial practical relevance for these devices as it can detect small magnetic changes against external stimuli, even when the ME coefficient is very weak [38,39]. This makes FMR a highly sensitive technique than other commercial facilities such as magneto-optic Kerr effect (MOKE) magnetometry, superconducting quantum interference device (SQUID), or vibrating sample magnetometer (VSM) [40]. Additionally, bidirectional magnetization switching to realize remote FMR tuning upward as well as downward is also not explored yet.

To address this problem, we studied the microwave performance of Ni/PMN-PT (FM/FE) magnetoelectric heterostructure during light-induced FMR tuning. Ni is selected as an FM layer because of its low FMR linewidth [41]. PMN-PT is chosen as a FE layer due to its superior photostrictive efficiency and high photoelastic coupling compared to conventional FEs such as SbSI, BFO Sm-BFO, etc. [26]. Additionally, PMN-PT exhibits the remarkable capability to respond to an extensive spectrum

of light frequencies, encompassing UV, IR, and extending all the way to the THz range [35]. This broadband response of PMN-PT is attributed to its unique band-to-band transition and crystal structure [42]. It is to be noted that PMN-PT demonstrates its peak photocurrent response near the ultraviolet (UV) range [33,34]. The much larger photocurrent observed near the UV region is associated with efficient band-to-band transitions [29,31,32]. This also suggests that there is faster momentum transfer near the UV range as corresponding UV light energy is closer to the band gap of the material. However, as the wavelength extends beyond the UV range and ventures into the infrared (IR) and terahertz (THz) ranges, the photocurrent reduces [35]. This is because the energy of the photons becomes lower and does not have enough energy to excite electrons across the band gap efficiently. Consequently, very few  $e-h$  pairs

are generated through band-to-band transitions, and the photocurrent generated in the IR range and beyond in PMN-PT is primarily attributed to the pyroelectric effect [35].

## II. EXPERIMENTAL DETAILS AND THEORETICAL INTERPRETATION

### A. Fabrication of ME heterostructure and measurement setup

The double-layer thin-film structure of Au(50 nm)/Ni(30 nm) (top electrode/FM) is deposited on the top side of 011-oriented single-crystal PMN-PT substrate (10 mm  $\times$  10 mm  $\times$  0.5 mm) using magnetron sputtering with a base pressure  $<10^{-6}$  Torr. Also, on the back side of PMN-PT, Au is deposited, which acts as a

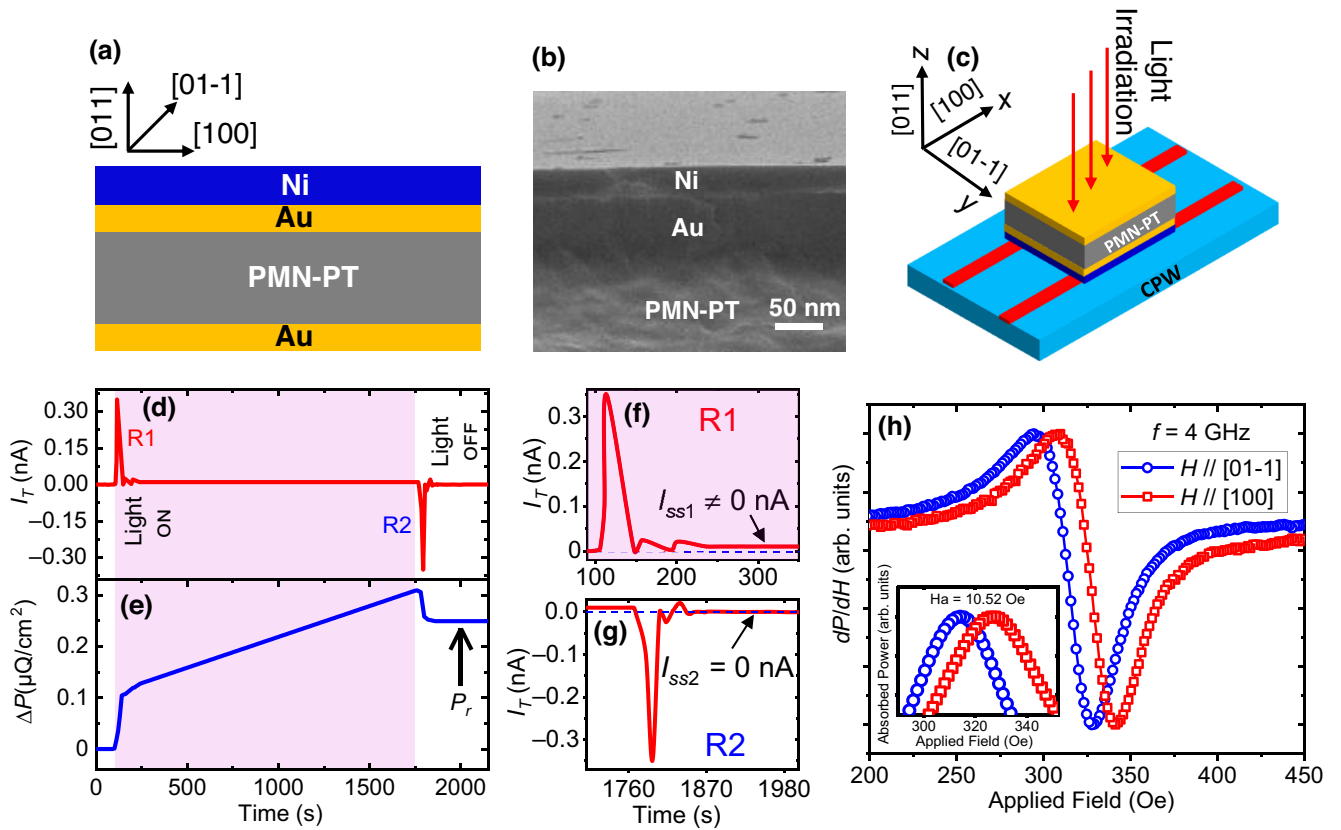


FIG. 1. (a) Schematic illustration of the Ni/PMN-PT magnetoelectric heterostructure with a coordinate system showing the crystalline direction of PMN-PT (not to scale). (b) Cross-section FESEM image of the heterostructure. (c) Schematics of the FMR measurement (not to scale). The sample is laid face down on CPW in flip-chip orientation, and light is irradiated along the [011] direction with the magnetic field applied along [01-1] or [100] directions. (d) TPC response of the PMN-PT under light irradiation and (e) corresponding remanent polarization obtained. (f) When light is switched ON, TPC with a positive peak is observed that decays to a nonzero steady-state value, i.e.,  $I_{SS1} \neq 0$  nA, as shown in region R1 of 1(d). (g) When light is switched OFF, TPC with a negative peak is observed that finally decays to zero, i.e.,  $I_{SS2} = 0$  nA as shown in region R2 of 1(d). (h) FMR absorption spectra change in the heterostructure without irradiating a light pulse under a magnetic field applied along different PMN-PT crystalline directions. The inset curve shows half-power absorbed power spectra. FMR absorption spectra change in the heterostructure without irradiating a light pulse under a magnetic field applied along different PMN-PT crystalline directions. The inset curve shows half-power absorbed power spectra. A small anisotropic field of 10.52 Oe is observed at 4 GHz due to residual stress from different lattice parameters along [01-1] and [100] crystalline directions.

bottom electrode. Figure 1(a) shows the schematic illustration of the fabricated ME heterostructure, with Fig. 1(b) showing the cross-section morphology of the heterostructure obtained using field emission scanning electron microscopy (FESEM). Figure 1(c) shows the schematics of the FMR measurement. The sample is laid face down on a co-planer waveguide (CPW) in flip-chip orientation, and light is irradiated along the [011] direction with the magnetic field applied along [01-1] or [100] directions during measurements. A continuous infrared (IR) light pulse of power  $100 \text{ W/m}^2$ , spot size diameter 10 mm, and wavelength 780 nm is used to irradiate the heterostructure, and no external bias voltage is used. Notably, the power consumption required to drive this light source is 7.8 mW. As a result, an internal electric field ( $E_i$ ) is created and the heterostructure exhibits the transient photocurrent (TPC) response, as shown in Fig. 1(d). TPC causes a change in the internal polarization of PMN-PT and, consequently, generates the piezostain [32]. It is worth noting that the IR range is opted instead of the UV range to ensure accurate and consistent measurements, given the limitations of the experimental setup.

### B. Light-induced magnetic field generation in Ni/PMN-PT

To illustrate the light-induced FMR shift, we first explore the underlying physics using mathematical analysis. For this, TPC measurement is carried out using the Keithley 4200A-SCS parameter analyzer. The nature of TPC is given by [36,37]

$$I_T(t) = I_p + \frac{Ap \Delta T_m}{\tau_\theta} \exp\left(\frac{-t}{\tau_\theta}\right), \quad (1)$$

where  $I_p$  is the steady-state photocurrent under light irradiation,  $A$  is the electrode area,  $p$  is the pyroelectric coefficient of PMN-PT,  $\Delta T_m$  is the maximum temperature variation of the PMN-PT under light irradiation, and  $\tau_\theta$  is the thermal time constant of PMN-PT. Initially, when the IR light is OFF, all internal electric dipoles of the PMN-PT substrate are oriented along  $\langle 111 \rangle$  direction and do not wiggle [36,37]. Once the IR light is ON, internal electric dipoles of the PMN-PT substrate start wiggling at a higher angle and lower the polarization of the PMN-PT substrate. This causes a reduction in bound surface charge ( $Q_s$ ). To balance  $Q_s$ , released surface charges ( $Q_r$ ) outflow, causing a TPC with a positive peak, as shown in region R1 of Fig. 1(d). Once the thermal equilibrium is achieved due to static charge balance, i.e.,  $Q_s = Q_r$ , TPC decays to a nonzero steady-state value, i.e.,  $I_T(t) = I_p = I_{ss1} \neq 0 \text{ nA}$ , as shown in Fig. 1(f). Alternatively, when the IR light is OFF, internal electric dipoles of the PMN-PT substrate start wiggling at a lower angle and increase the polarization of the PMN-PT substrate. This causes an increase in

bound surface charge ( $Q_s$ ). To balance  $Q_s$ , released surface charges ( $Q_r$ ) outflow, causing a TPC with a negative peak, as shown in region R2 of Fig. 1(d). Once the thermal equilibrium is achieved due to static charge balance, TPC finally decays to zero, i.e.,  $I_T(t) = I_{ss2} = 0 \text{ nA}$ , as shown in Fig. 1(g).

Next, using the polarization relaxation equation [43] change in internal polarization ( $\Delta P(t)$ ) of the PMN-PT is calculated, as shown in Fig. 1(e)

$$\Delta P(t) = P(t) - P(0) = \frac{1}{A\epsilon} \int_0^{t_i} I_T(t) dt, \quad (2)$$

where  $P(t)$  and  $P(0)$  are the polarization at time  $t$  and  $t = 0$  sec, respectively.  $\epsilon$  is the permittivity of PMN-PT and  $t_i$  is the irradiation time. Using Eqs. (1) and (2) modified as

$$\Delta P(t) = \frac{1}{A\epsilon} \left[ I_p(t_i) + Ap \Delta T_m \left( 1 - \exp\left(\frac{-t_i}{\tau_\theta}\right) \right) \right]. \quad (3)$$

It is evident from Eq. (3) that the steady-state photocurrent ( $I_p$ ) results in an increase in polarization. When the light is switched OFF, polarization persists slightly, resulting in a remanent polarization state ( $P_r$ ) and different polarization states can be obtained from different irradiation times ( $t_i$ ), as shown in Fig. 2(a). This polarization change of PMN-PT under light irradiation is the primary order parameter that generates the time-dependent piezostain ( $s(t)$ ). To quantify  $s(t)$  and its nature under light irradiation, the photoinduced resistance measurement method is employed. This relationship is mathematically described by

$$\frac{\Delta R}{R} = \Gamma \frac{\Delta L}{L}, \quad (4)$$

where,  $\Delta R/R$  represents the fractional photoresistance change, and  $\Delta L/L = \Delta s(t)$  denotes the time-dependent strain change. The parameter  $\Gamma$  represents the photostrictive coefficient, characterizing the correlation between strain and light-induced resistance changes. A Keithley 6221 current source and a Keithley 2182 nanovoltmeter are used for the photoresistance measurement. Upon light irradiation, an increase in photoresistance is observed with respect to the time, as shown in the region R1 of Fig. 2(b). Since the photostrictive coefficient remains constant for a given material, the strain change can be calculated using Eq. (4), as shown on the right ordinate of Fig. 2(b). However, after switching OFF the light source, the ferroelastic domains gradually relaxed to another equilibrium configuration, leading to the appearance of remanent photoresistance ( $R_r$ ). This remanent photoresistance ( $R_r$ ) is directly related to the remanent photostriction in the material [32]. It is worthwhile to note that this remanent photostriction exhibited volatile behavior, implying that it is not a stable or long-lasting effect, as shown in region R2 of

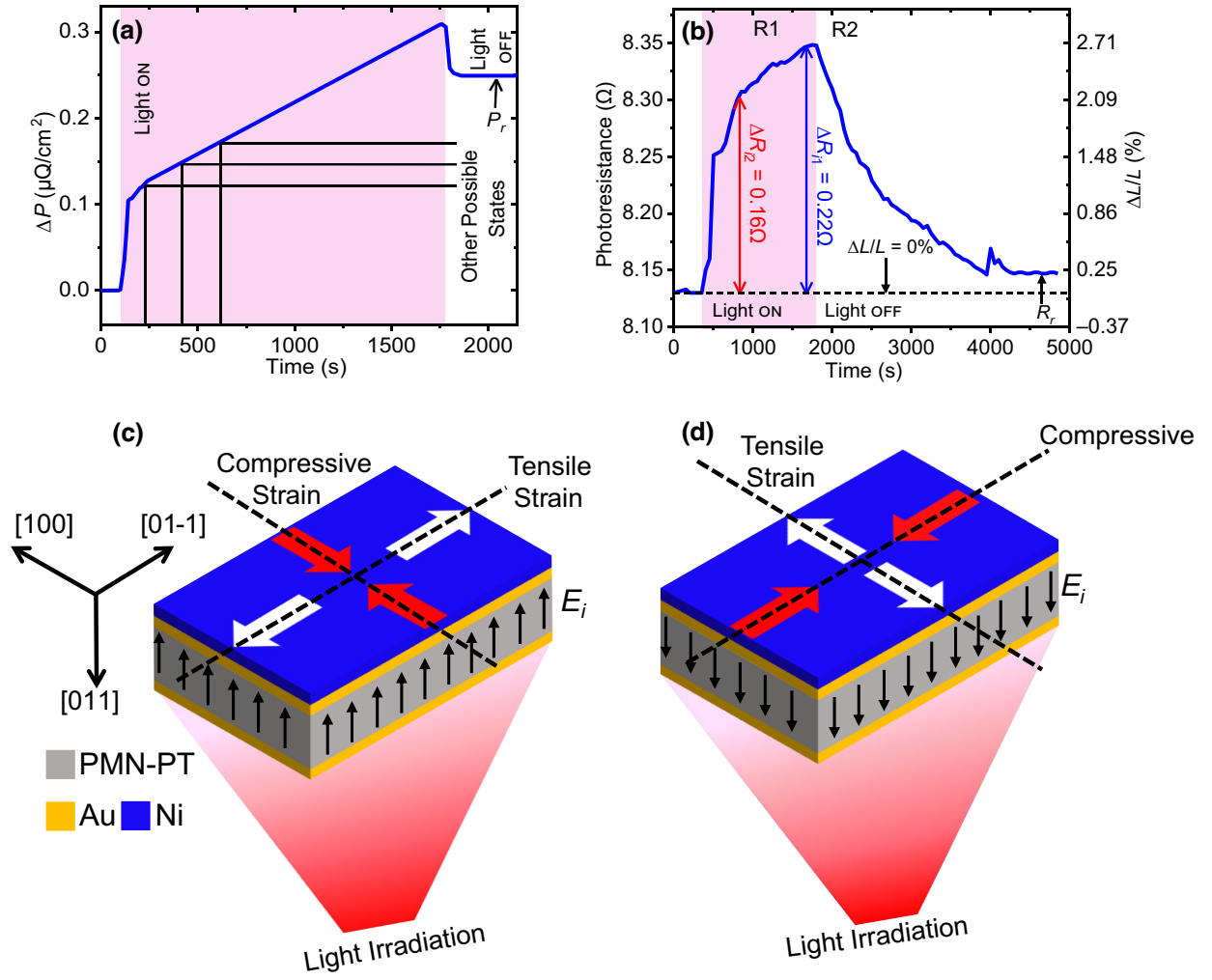


FIG. 2. (a) Possible remanent polarization states at different irradiation time. (b) Light-induced photoresistance change of Ni/PMN-PT ME heterostructure for different irradiation times. Light-induced tensile (01-1) and compressive strain (100) generation in Ni thin film. (c) The generated piezostrain would have tensile and compressive strain components along [01-1] and [100] crystalline directions of PMN-PT, respectively, if developed  $E_i$  is positive in nature. (d) The generated piezostrain would have tensile and compressive strain components along [100] and [01-1] crystalline directions of PMN-PT, if developed  $E_i$  is negative in nature.

Fig. 2(b). This time-dependent piezostrain instigates the effective magnetic anisotropy in the FM layer and subsequently controls the spin magnetic moment. Light-induced effective magnetic field ( $H_{\text{eff}}$ ) can be expressed as

$$H_{\text{eff}} = \frac{3\lambda Y s(t)}{\mu_0 M_s}, \quad (5)$$

where  $\lambda$ ,  $Y$ , and  $M_s$  are the magnetostrictive coefficient, Young's modulus, and saturation magnetization of the FM layer, respectively.  $\mu_0$  is the vacuum permeability. This light-induced effective magnetic field described in Eq. (5) lays the foundation for FMR manipulation as described in the Kittel equation [3]

$$f = \gamma \sqrt{(H_r + H_{\text{eff}})(H_r + H_{\text{eff}} + 4\pi M_s)} \quad (6)$$

where  $f$ ,  $\gamma$ , and  $H_r$  are the in-plane FMR frequency, gyromagnetic ratio, resonance magnetic field, respectively.

### III. RESULTS AND DISCUSSION

#### A. Light-induced FMR modulation in Ni/PMN-PT

Next, light-induced FMR modulations in Ni/PMN-PT heterostructure are illustrated using a CPW FMR measurement unit, as shown in Fig. 1(c). The sample is laid face down on a CPW, and measurements are performed in LT (magnetized longitudinal and polarized transverse) mode. It is to be noted that the obtained piezostrain [ $s(t)$ ] by 011-cut PMN-PT when irradiated along the transverse ([011]) direction is biaxial in nature, having longitudinal tensile and compressive strain components. As Ni is a negative magnetostrictive material, the direction of strain

components will depend on the nature of  $E_i$ . The generated piezostain would have tensile and compressive strain components along [01-1] and [100] crystalline directions of PMN-PT, respectively, if developed  $E_i$  is positive due to photovoltaic effect under light irradiation [20,21], as shown in Fig. 2(c). On the other hand,  $s(t)$  would have tensile and compressive strain components along [100] and [01-1], respectively, if generated  $E_i$  is negative in nature [20,21], as shown in Fig. 2(d). Interestingly, a small anisotropic field is also observed without irradiating a light pulse when an external magnetic field is applied along different PMN-PT crystalline directions, as shown in Fig. 1(h). This is because of the generated residual stress from different lattice parameters along [01-1] and [100] crystalline directions of the PMN-PT substrate [17].

Figure 3 shows the light-induced dependence of the FMR absorption spectra in field-sweeping mode when the external magnetic field is applied along [01-1] and [100] at different FMR frequencies. Upon irradiating the IR light on a sample, an upward resonance field shifts ( $H_{\text{shift}} > 0$ ) is observed when the external magnetic field ( $H$ ) is applied along the [01-1] direction, as shown in Fig. 3(a). This is because, for negative magnetostrictive materials according to Eq. (5), the generated light-induced piezostain produces

the compressive strain along [01-1] directions and induces a negative  $H_{\text{eff}}$ . A negative  $H_{\text{eff}}$  causes the magnetization to align perpendicular to the anisotropic field, which leads to the misalignment between the magnetization and the anisotropy axis. Consequently, the generated demagnetizing field increases. Since the external magnetic field is also applied along [01-1] direction and  $H_{\text{eff}}$  in the Kittel equation takes into account the generated demagnetizing field also, an upward resonance field shift is observed according to Eq. (6). On the other hand, a downward resonance field shift ( $H_{\text{shift}} < 0$ ) is observed when the external magnetic field is applied along the [100] direction, as shown in Fig. 3(b). The downward shift occurs as the light-induced piezostain generates the tensile strain along [100] direction and induces a positive  $H_{\text{eff}}$ . A positive  $H_{\text{eff}}$  causes the magnetization to align parallel to the anisotropic field, which reduces the generated demagnetizing field. Since the external magnetic field is also applied along [100] direction, a downward resonance field shift is observed. Comparing to the previously published work based on electric field control of FMR for negative magnetostrictive materials,  $s(t)$  would have tensile and compressive strain components along [100] and [01-1], respectively, if generated  $E_i$  is negative in nature [15–18,20,21]. This

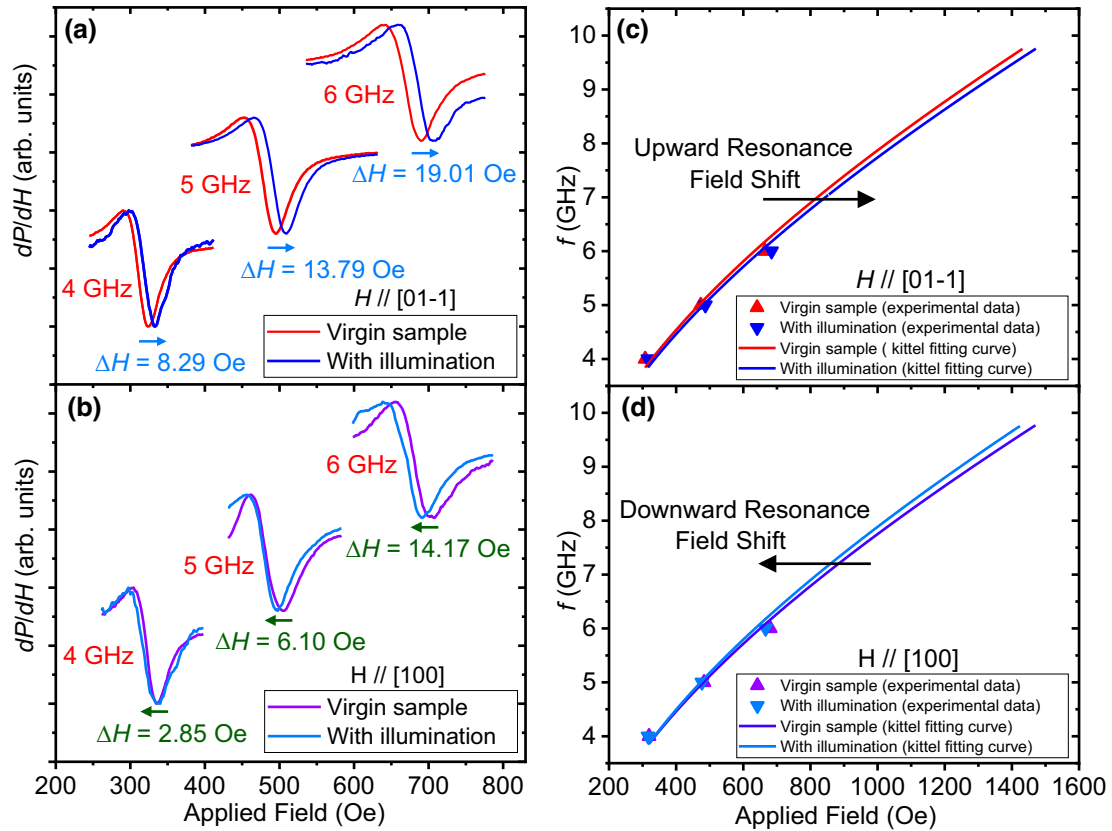


FIG. 3. FMR absorption spectra change in the heterostructure under light pulse when the magnetic field is applied along (a) tensile strain [01-1] and (b) compressive strain [100] direction of PMN-PT at different FMR frequencies. (c),(d) show corresponding upward and downward, respectively. In both cases symbols show experimental points and solid curves are fitted using the Kittel equation.

suggests that IR light acts as a negative  $E_i$  in the light-induced FMR absorption spectra in the Ni/PMN-PT heterostructure. Figures 3(c) and 3(d) show the corresponding fitted curve using the Kittel equation [Eq. (6)], where theoretical and experimental calculations fit well. Figure 4(a) summarizes the results obtained and suggests the bidirectional magnetization switching due to the cooperation between magnetic field orientation and applied light pulse. Using the FMR absorption spectra, FWHM is also calculated to obtain the FMR linewidths ( $\Delta H$ ), as shown in Fig. 4(b). It is observed that the Ni thin film perpetuates FMR absorption spectra for small linewidths even after applying a light pulse, with a change in linewidth  $< 10$  Oe. This suggests uniform deformation in Ni thin film due to the generated biaxial piezostain [18]. (See Appendix A for discussions on FMR spectra fitting, extraction of the resonance field, and linewidth calculation.)

To explore the light-induced magnetic relaxation in the sample, frequency-dependent linewidth ( $\Delta H$ ) is fitted using the linewidth equation [44], as shown in Fig. 4(c). When the magnetic field is applied along [01-1] direction of PMN-PT, upon light irradiation, a slight increase in the damping coefficient ( $\alpha(\pm\delta\alpha)$ ) from  $0.03247(\pm 0.0062)$  to  $0.03487(\pm 0.00252)$  is observed, where  $\delta\alpha$  represents the error corresponding to the  $\alpha$  measurement. This change implies a shorter relaxation time, indicating that the system returns to equilibrium more quickly following light-induced perturbation. This also suggests a more efficient energy exchange between magnetic moments and lattice vibrations. On the other hand, when the magnetic field is applied along the [100] direction of PMN-PT, and light is irradiated, a slight reduction in  $\alpha$  from  $0.01313(\pm 0.0013)$  to  $0.01271(\pm 0.00129)$  is observed. This decrease implies a longer relaxation time, indicating that the system retains its perturbed state energy for an extended period before returning to equilibrium during FMR upon light irradiation in this case. The reduced damping coefficient also suggests a slightly less efficient energy exchange between magnetic moments and lattice vibrations, resulting in slower energy dissipation in this case. (See Appendices B and C for discussions on damping parameter calculation using linewidth equation, and error calculation for  $H_{\text{shift}}$ , respectively.)

It is worth noting that a downward resonance field shift indicates that the driving mechanism for the observed FMR shift is light-induced piezostain rather than direct thermal excitation of the FM layer. This is evident from the fact that the thermal excitation causes a reduction in magnetization of FM due to increasing excitation of spin waves given by Bloch  $T^{3/2}$  law [45,46] so that only an upward FMR shift is possible, obtained using modified Bloch law [47,48]

$$H(T)_{\text{shift}} = H_{\text{res}}(0)[HT^{3/2}], \quad (7)$$

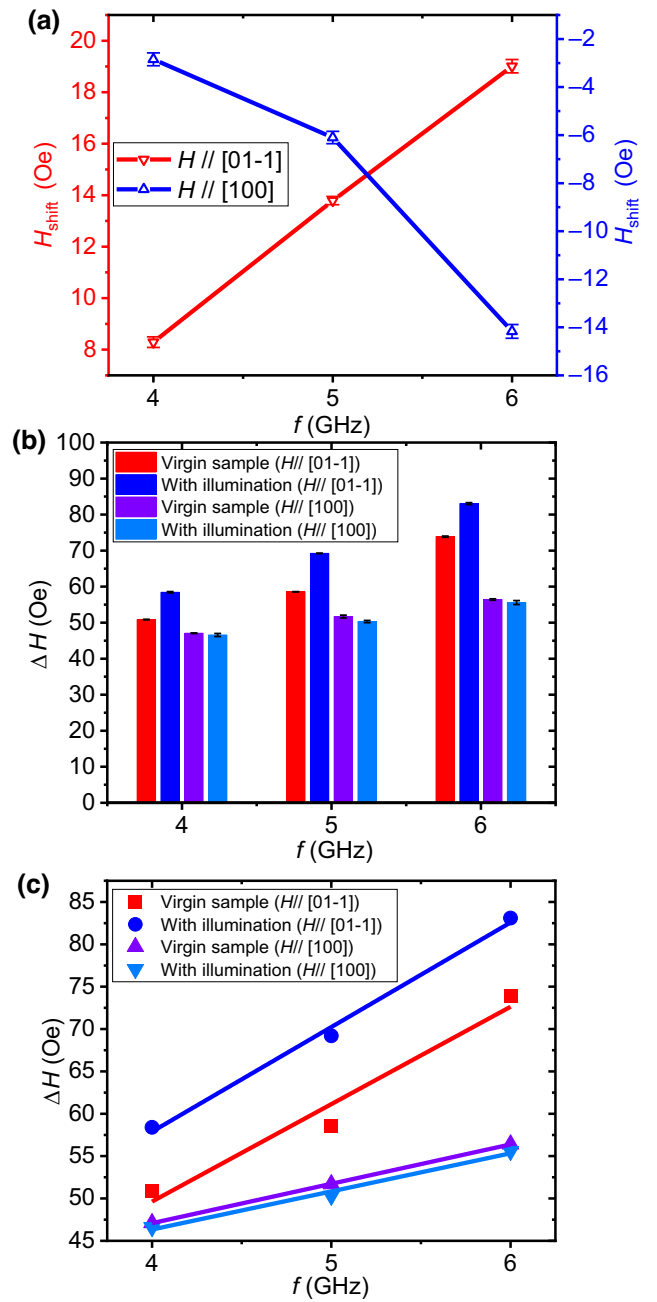


FIG. 4. (a) The induced bidirectional magnetic field shift due to the cooperation between magnetic field orientation and applied light pulse. (b) FMR linewidth variation against FMR frequency in the virgin sample and the sample under light irradiation when the magnetic field is applied along [01-1] and [100] directions, respectively. (c) Light-induced damping parameter calculation. In each case, symbols show experimental points and solid curves are fitted using the linewidth equation.

where  $H(T)_{\text{shift}}$ ,  $H_{\text{res}}(0)$ ,  $H$ , and  $T$  are temperature-dependent resonance field shift, resonance field at  $T = 0$  K, external applied magnetic field, and external temperature, respectively.

## B. Effect of irradiation time

To further study how irradiation time can also manipulate the FMR, the effect of  $t_i$  on FMR absorption spectra is illustrated next. As it is evident from Eq. (3) that different polarization states can be obtained from different  $t_i$ , the TPC response of PMN-PT under constant illumination for two different illumination times is recorded. As the total external field sweep time ( $t_{\text{sweep}}$ ) during FMR measurements is approximately equal to 28 min; first, the TPC response of PMN-PT is obtained for  $t_{i1} = t_{\text{sweep}} = 28$  min [Fig. 5(a)]. Figure 5(b) shows the corresponding peak value of the polarization change ( $\Delta P \approx 0.31 \mu\text{C}/\text{cm}^2$ ) calculated using Eq. (2). Next, the irradiating time is reduced to half, i.e.,  $t_{i2} = t_{\text{sweep}}/2 = 14$  min. TPC shows the same peak current as the irradiation power is constant [Fig. 5(c)]. However, the peak value of  $\Delta P$  reduces to approximately equal to  $0.17 \mu\text{C}/\text{cm}^2$ , as shown in Fig. 5(d). This suggests that polarization change is related approximately linearly to irradiation time, considering the subcoercive region operation of PMN-PT. Based on this, FMR modulations in Ni/PMN-PT heterostructure for  $t_{i1} = 28$  min and  $t_{i2} = 14$  min are obtained at  $f = 5$  GHz when the external magnetic field is applied along [01-1], as shown in Fig. 5(e). As the increase in irradiation time increases  $\Delta P$  [Fig. 2(a)], generated piezostain [ $s(t)$ ] in PMN-PT also increases, as shown in Fig. 2(b). For instance, a fractional change in resistance  $\Delta R_{i2} = 0.16\Omega$  is observed for  $t_{i2} = 14$  min, while extending the illumination time to 28 min, resulted in a fractional change in resistance of  $\Delta R_{i1} = 0.22 \Omega$ , as shown in Fig. 2(b). Consequently, light-induced effective magnetic field ( $H_{\text{eff}}$ ) in the Ni film increases with  $s(t)$  provided the subcoercive region operation of PMN-PT. This is because,  $\lambda$ ,  $Y$ , and  $\mu_0$  are constant in Eq. (5), while remanence ratio ( $M_r/M_s$ ) exhibited negligible change under light irradiation as reported by Zhang *et al.* [33] and Dagur *et al.* [34]. This signifies that  $H_{\text{eff}}$  could exhibit almost a similar trend as  $s(t)$  considering negligible change in  $M_s$ . Since the external magnetic field is applied along [01-1] direction an upward resonance field shift is observed with increasing  $t_i$ , as shown in Fig. 5(e). This suggests that higher  $H_{\text{eff}}$  can also be induced in the FM layer by increasing the irradiation time, even though illumination power is constant. Also, almost the same linewidth is observed at different  $t_i$ , as shown in half-power absorbed power spectra in the inset of Fig. 5(e). This also confirms the linear deformation in the Ni thin film with an increase in  $t_i$ . It is to be noted that increasing the irradiation power will also result in an increase in the modulation of FMR. This is attributed to the heightened absorption of photons by the material with increased irradiation power, which subsequently leads to generating more electron-hole pairs [26,31]. Additionally, this augmented photon absorption contributes to more localized heating of the ferroelectric material [35]. As a direct

consequence, a higher photocurrent is generated. The generated photocurrent leads to a corresponding increase in the piezostain induced by the photostriction. Considering this the experiments are carried out utilizing the maximum available irradiation power. However, it is important to consider that there will be a limit where the strain in the PMN-PT reaches a certain saturation point, beyond which further exposure to higher irradiation power may not significantly increase the generated piezostain. This behavior is akin to the electric field modulation in PMN-PT, as demonstrated by Choi *et al.* [49], where the piezostain reaches a saturated point for an electric field of 0.5 MV/m, attributed to a morphotropic phase transition in the PMN-PT.

## C. Volatile FMR nature

Since, in FE materials, the polarization-electric field ( $P$ - $E$ ) loop provides a comprehensive depiction of the intricate relationship between polarization and its directional response to the electric field,  $P$ - $E$  loop characterization is conducted, as shown in Fig. 5(f). It is evident from Fig. 2(a) different remanent polarization ( $P_r$ ) states could be induced due to the generated internal electric field for varying illumination times. This leads to slight displacements of the ferroelastic domains in PMN-PT and causes some deformation even after the light is switched OFF [26,32]. For instance, in Fig. 5(b),  $P_r = 0.25 \mu\text{C}/\text{cm}^2$  is observed after the light is switched OFF following the maximum sweep time ( $t_{\text{sweep}} = 28$  min) light irradiation. However, it is essential to note that the remanent polarization, which remains even after the light is switched OFF, is significantly smaller when compared to the saturation polarization ( $P_{\text{sat}} = 22 \mu\text{C}/\text{cm}^2$ ) of PMN-PT, as shown in Fig. 5(d). The fact that  $P_r \ll P_{\text{sat}}$  strongly suggests that the internal electric field generated under light illumination is insufficient to fully saturate the polarization of the FE material. From Fig. 5(f), it is also evident that the corresponding electric field required to achieve a polarization change of  $0.25 \mu\text{C}/\text{cm}^2$  from its initial polarization state [indicated as the transition from point 1 ( $P(0)$ ) to point 2 ( $P(t)$ )] is only 0.06 MV/m. The experimental findings suggest that to achieve a polarization change of  $0.25 \mu\text{C}/\text{cm}^2$  in PMN-PT, an internal electric field of 0.06 MV/m is required under light illumination. This observation clarifies that the light-induced internal electric field ( $E_i$ ) is still smaller than the coercive electric field of PMN-PT ( $E_c = 0.5$  MV/m), which is the minimum electric field required to switch the polarization direction of FE material. Consequently, the nonvolatile FMR nature is not observed. Contradictory electric field control of FMR reported earlier is nonvolatile if the applied electric field is greater than  $E_c$  of the PE substrate [15–18].



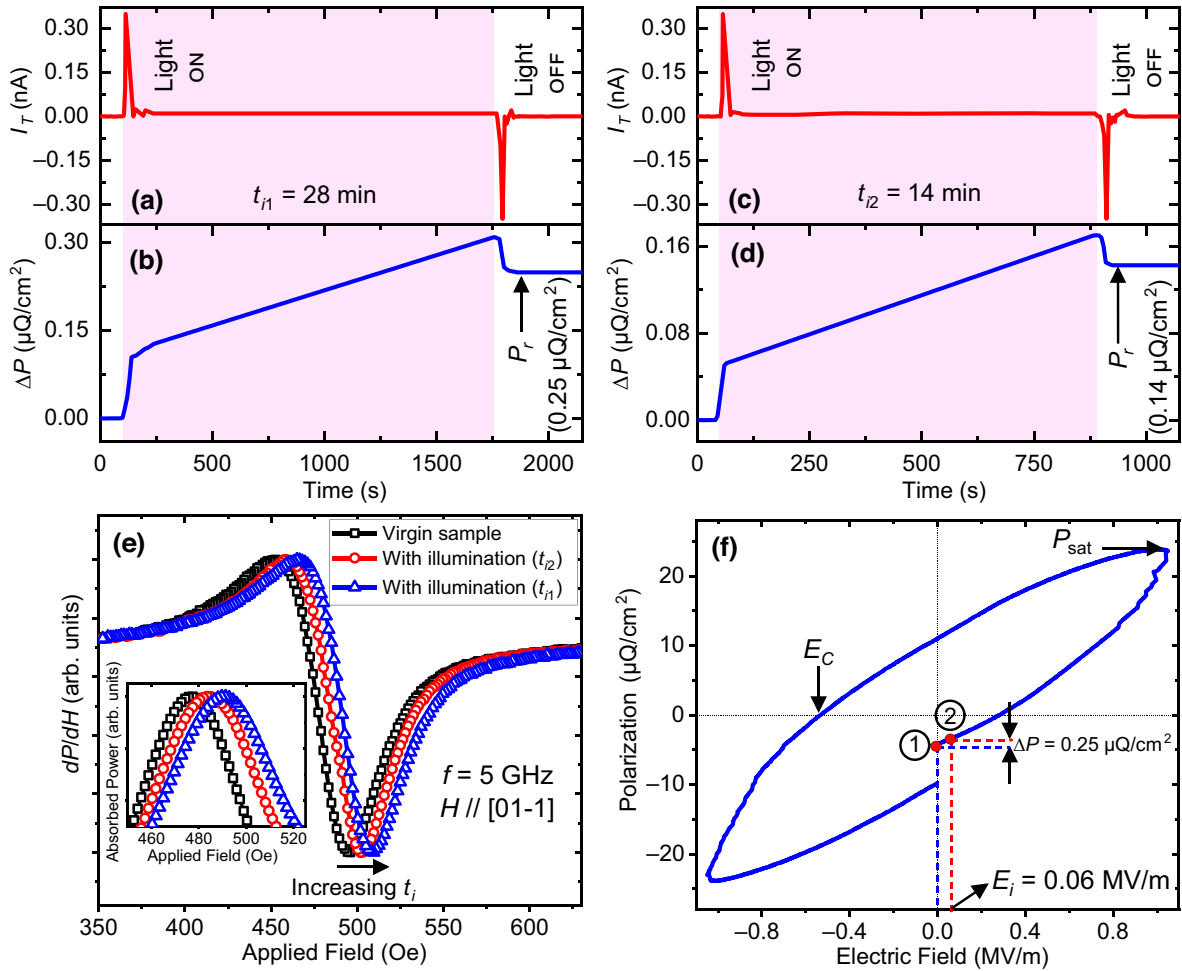


FIG. 5. Effect of illumination time on remanent polarization and FMR absorption spectra. (a) TPC response of PMN-PT under constant illumination for 28 min and (b) corresponding remanent polarization obtained. (c) TPC response of PMN-PT under continuous illumination for 14 min and (d) corresponding remanent polarization obtained. (e) FMR absorption spectra upward shift due to a change in illumination time at a FMR frequency of 5 GHz when the magnetic field is applied along tensile strain ([01-1]) direction. The inset curve shows half-power absorbed power spectra at different illumination times. (f)  $P$ - $E$  loop characteristics of PMN-PT substrate.

#### IV. CONCLUSION

In conclusion, light-induced FMR tunability in Ni/PMN-PT magnetolectric heterostructure is demonstrated. It is observed that light causes a change in the internal polarization of PMN-PT and, consequently, generates the piezotrain, which is used to instigate the effective magnetic anisotropy in Ni thin film. Depending on the direction of the external applied magnetic field with respect to the PMN-PT crystalline directions, upward and downward volatile FMR shift is obtained. Finally, it is shown that higher effective magnetic anisotropy in Ni thin film can also be induced by increasing the irradiation time at constant illumination power. This work can provide a framework for next-generation light-controlled ME-based rf and microwave devices. Such methods could also facilitate better integration and scalability of ME-based microwave devices by eliminating the need for direct electrical

contacts or bulky external components, thus allowing an easier integration into complex device architectures. Additionally, such a method can lead to a reduction in the dimensions of ME-based microwave devices that could be beneficial for portable and energy-efficient device applications.

#### ACKNOWLEDGMENTS

This work is financially supported by International Bilateral Corporation Division of the Department of Science and Technology (DST), Government of India, under Indo-Norway joint project (Project No. INT/NOR/RCN/NS/P-06/2019). The authors acknowledge NRF and CRF, IIT Delhi, for providing fabrication and characterization facilities. The authors thank Professor Sujeet Chaudhary, Department of Physics, IIT Delhi for allowing us to use lab facilities for FMR measurements.

### APPENDIX A

The FMR spectra is recorded with an external magnetic field applied along [01-1] and [100] crystalline directions of PMN-PT at different FMR frequencies (4–6 GHz). The obtained FMR signal ( $V_{\text{FMR}}$ ) is fitted using Lorentzian function derivative given by [50]

$$V_{\text{FMR}} = -A \frac{[(0.5\delta)^2(H_{\text{ext}} - H_r)]}{[(0.5\delta)^2 + (H_{\text{ext}} - H_r)^2]^2} + B \frac{(0.5\delta)[(0.5\delta)^2 - (H_{\text{ext}} - H_r)^2]}{[(0.5\delta)^2 + (H_{\text{ext}} - H_r)^2]^2}, \quad (\text{A1})$$

where  $A$  and  $B$  are symmetric and antisymmetric absorption coefficients.  $\delta$ ,  $H_r$ , and  $H_{\text{ext}}$  are linewidth, resonance field, and external applied magnetic field, respectively. Using Eq. (A1), the resonance magnetic field and the linewidth for each in-plane FMR frequency is obtained. Linewidth is calculated as the FWHM of the spectra response.

### APPENDIX B

To explore the light-induced magnetic relaxation in the sample, frequency-dependent linewidth ( $\Delta H$ ) is fitted using linewidth equation [44] given by

$$\Delta H = \Delta H_0 + \frac{\alpha f}{\gamma} \quad (\text{B1})$$

where  $\Delta H_0$  is characterized by being frequency-independent, typically emerging as a consequence of various factors, including magnetic inhomogeneity phenomena, imperfections in the sample, and extrinsic contributions that are not related to the energy dissipation processes during FMR [44]. The second term,  $\alpha f / \gamma$  represents a frequency-dependent mechanism governing magnetization relaxation and accounts for the energy dissipation due to damping during FMR [44]. Here  $\alpha$  represents a damping parameter,  $\gamma$  is gyromagnetic ratio, and  $f$  signifies the microwave frequency.

### APPENDIX C

To calculate the error in the magnetic field shift ( $\delta H_{\text{shift}}$ ) error propagation formula is used. For this square root of the sum of the squares of the individual errors in the magnetic field measurements are used as follows:

$$\delta H_{\text{shift}} = \sqrt{(\delta H_r)^2 + (\delta H_{ri})^2}, \quad (\text{C1})$$

where  $\delta H_r$  represents the error corresponding to the resonance magnetic field of the virgin sample and  $\delta H_{ri}$  error corresponds to the resonance magnetic field of the sample subjected to light illumination.

- [1] J. Grollier, D. Querlioz, K. Camsari, K. Everschor-Sitte, S. Fukami, and M. D. Stiles, Neuromorphic spintronics, *Nat. Electron.* **3**, 360 (2020).
- [2] J.-G. Choi, J. Park, M.-G. Kang, D. Kim, J.-S. Rieh, K.-J. Lee, K.-J. Kim, and B.-G. Park, Voltage-driven gigahertz frequency tuning of spin hall nano-oscillators, *Nat. Commun.* **13**, 3783 (2022).
- [3] C. Kittel, Interpretation of anomalous Larmor frequencies in ferromagnetic resonance experiment, *Phys. Rev.* **71**, 270 (1947).
- [4] M. Romera, P. Talatchian, S. Tsunegi, F. Abreu Araujo, V. Cros, P. Bortolotti, J. Trastoy, K. Yakushiji, A. Fukushima, and H. Kubota, *et al.*, Vowel recognition with four coupled spin-torque nano-oscillators, *Nature* **563**, 230 (2018).
- [5] D. Vodenicarevic, N. Locatelli, F. Abreu Araujo, J. Grollier, and D. Querlioz, A nanotechnology-ready computing scheme based on a weakly coupled oscillator network, *Sci. Rep.* **7**, 1 (2017).
- [6] T. Nozaki, Y. Shiota, S. Miwa, S. Murakami, F. Bonell, S. Ishibashi, H. Kubota, K. Yakushiji, T. Saruya, and A. Fukushima, *et al.*, Electric-field-induced ferromagnetic resonance excitation in an ultrathin ferromagnetic metal layer, *Nat. Phys.* **8**, 491 (2012).
- [7] F. Giesen, J. Podbielski, T. Korn, M. Steiner, A. Van Staa, and D. Grundler, Hysteresis and control of ferromagnetic resonances in rings, *Appl. Phys. Lett.* **86**, 112510 (2005).
- [8] Y. Chen, M. J. Nedoroscik, A. L. Geiler, C. Vittoria, and V. G. Harris, Perpendicularly oriented polycrystalline BaFe<sub>11.1</sub>Sc<sub>0.9</sub>O<sub>19</sub> hexaferrite with narrow FMR linewidths, *J. Am. Ceram. Soc.* **91**, 2952 (2008).
- [9] S. Iihama, T. Taniguchi, K. Yakushiji, A. Fukushima, Y. Shiota, S. Tsunegi, R. Hiramatsu, S. Yuasa, Y. Suzuki, and H. Kubota, Spin-transfer torque induced by the spin anomalous Hall effect, *Nat. Electron.* **1**, 120 (2018).
- [10] S. I. Kiselev, J. Sankey, I. Krivorotov, N. Emley, R. Schoelkopf, R. Buhrman, and D. Ralph, Microwave oscillations of a nanomagnet driven by a spin-polarized current, *Nature* **425**, 380 (2003).
- [11] A. Tulapurkar, Y. Suzuki, A. Fukushima, H. Kubota, H. Maehara, K. Tsunekawa, D. Djayaprawira, N. Watanabe, and S. Yuasa, Spin-torque diode effect in magnetic tunnel junctions, *Nature* **438**, 339 (2005).
- [12] J. C. Slonczewski, Current-driven excitation of magnetic multilayers, *J. Magn. Magn. Mater.* **159**, L1 (1996).
- [13] G. E. Bauer, E. Saitoh, and B. J. Van Wees, Spin caloritronics, *Nat. Mater.* **11**, 391 (2012).
- [14] H. Yu, S. Granville, D. Yu, and J.-P. Ansermet, Evidence for thermal spin-transfer torque, *Phys. Rev. Lett.* **104**, 146601 (2010).
- [15] M. Liu, O. Obi, J. Lou, Y. Chen, Z. Cai, S. Stoute, M. Espanol, M. Lew, X. Situ, and K. S. Ziemer, *et al.*, Giant electric field tuning of magnetic properties in multiferroic ferrite/ferroelectric heterostructures, *Adv. Funct. Mater.* **19**, 1826 (2009).
- [16] J. Lou, M. Liu, D. Reed, Y. Ren, and N. X. Sun, Giant electric field tuning of magnetism in novel multiferroic FeGaB/lead zinc niobate–lead titanate (PZN-PT) heterostructures, *Adv. Mater.* **21**, 4711 (2009).

- [17] M. Liu, B. M. Howe, L. Grazulis, K. Mahalingam, T. Nan, N. X. Sun, and G. J. Brown, Voltage-impulse-induced non-volatile ferroelastic switching of ferromagnetic resonance for reconfigurable magnetoelectric microwave devices, *Adv. Mater.* **25**, 4886 (2013).
- [18] M. Liu, Z. Zhou, T. Nan, B. M. Howe, G. J. Brown, and N. X. Sun, Voltage tuning of ferromagnetic resonance with bistable magnetization switching in energy-efficient magnetoelectric composites, *Adv. Mater.* **25**, 1435 (2013).
- [19] N. A. Spaldin and R. Ramesh, Advances in magnetoelectric multiferroics, *Nat. Mater.* **18**, 203 (2019).
- [20] P. Pathak and D. Mallick, Size-dependent magnetization switching in magnetoelectric heterostructures for self-biased MRAM applications, *IEEE Trans. Electron Devices* **68**, 4418 (2021).
- [21] P. Pathak and D. Mallick, Straintronic nanomagnetic logic using self-biased dipole coupled elliptical nanomagnets, *IEEE Trans. Magn.* **58**, 1 (2022).
- [22] P. Pathak, V. K. Yadav, and D. Mallick, Deterministic domain wall rotation in a strain mediated FeGaB/PMN-PT asymmetrical ring structure for manipulating trapped magnetic nanoparticles in a fluidic environment, *RSC Adv.* **13**, 2820 (2023).
- [23] N. Murali, S. K. Rainu, N. Singh, and S. Betal, Advanced materials and processes for magnetically driven micro- and nano-machines for biomedical application, *Biosens. Bioelectron. X* **11**, 100206 (2022).
- [24] T. Wu, A. Bur, K. Wong, J. Leon Hockel, C.-J. Hsu, H. K. Kim, K. L. Wang, and G. P. Carman, Electric-poling-induced magnetic anisotropy and electric-field-induced magnetization reorientation in magnetoelectric Ni/(011)[Pb(Mg<sub>1/3</sub>Nb<sub>2/3</sub>)O<sub>3</sub>]<sub>(1-x)</sub>-[PbTiO<sub>3</sub>]<sub>x</sub> heterostructure, *J. Appl. Phys.* **109**, 07D732 (2011).
- [25] T. Wu, A. Bur, K. Wong, P. Zhao, C. S. Lynch, P. K. Amiri, K. L. Wang, and G. P. Carman, Electrical control of reversible and permanent magnetization reorientation for magnetoelectric memory devices, *Appl. Phys. Lett.* **98**, 262504 (2011).
- [26] B. Kundys, Photostrictive materials, *Appl. Phys. Rev.* **2**, 011301 (2015).
- [27] S. Yang, J. Seidel, S. Byrnes, P. Shafer, C.-H. Yang, M. Rossell, P. Yu, Y.-H. Chu, J. Scott, and J. Ager III, *et al.*, Above-bandgap voltages from ferroelectric photovoltaic devices, *Nat. Nanotechnol.* **5**, 143 (2010).
- [28] I. Tatsuzaki, K. Itoh, S. Ueda, and Y. Shindo, Strain along *c* axis of SbSi caused by illumination in dc electric field, *Phys. Rev. Lett.* **17**, 198 (1966).
- [29] B. Kundys, M. Viret, D. Colson, and D. O. Kundys, Light-induced size changes in BiFeO<sub>3</sub> crystals, *Nat. Mater.* **9**, 803 (2010).
- [30] W. Jin Hu, Z. Wang, W. Yu, and T. Wu, Optically controlled electroresistance and electrically controlled photovoltage in ferroelectric tunnel junctions, *Nat. Commun.* **7**, 10808 (2016).
- [31] A. S. Makhort, F. Chevrier, D. Kundys, B. Doudin, and B. Kundys, Photovoltaic effect and photopolarization in Pb(Mg<sub>1/3</sub>Nb<sub>2/3</sub>)<sub>0.68</sub>Ti<sub>0.32</sub>O<sub>3</sub> crystal, *Phys. Rev. Mater.* **2**, 012401 (2018).
- [32] V. Iurchuk, D. Schick, J. Bran, D. Colson, A. Forget, D. Halley, A. Koc, M. Reinhardt, C. Kwamen, N. A. Morley, M. Bargheer, M. Viret, R. Gumeniuk, G. Schmerber, B. Doudin, and B. Kundys, Optical writing of magnetic properties by remanent photostriction, *Phys. Rev. Lett.* **117**, 107403 (2016).
- [33] X. Zhang, X. Guo, B. Cui, J. Yun, J. Mao, Y. Zuo, and L. Xi, Light modulation of magnetization switching in PMN-PT/Ni heterostructure, *Appl. Phys. Lett.* **116**, 132405 (2020).
- [34] D. Dagur, V. Polewczyk, A. Y. Petrov, P. Carrara, M. Brioschi, S. Fiori, R. Cucini, G. Rossi, G. Panaccione, and P. Torelli, *et al.*, Visible light effects on photostrictive/magnetostrictive PMN-PT/Ni heterostructure (Adv. Mater. Interfaces 36/2022), *Adv. Mater. Interfaces* **9**, 2270196 (2022).
- [35] H. Fang, C. Xu, J. Ding, Q. Li, J.-L. Sun, J.-Y. Dai, T.-L. Ren, and Q. Yan, Self-powered ultrabroadband photodetector monolithically integrated on a PMN-PT ferroelectric single crystal, *ACS Appl. Mater. Interfaces* **8**, 32934 (2016).
- [36] P. Pathak, V. K. Yadav, S. Das, and D. Mallick, Infrared-driven pyroelectric effect in magnetoelectric sensor for suspended on-chip magnetic nanoparticles quantification, *Appl. Phys. Lett.* **122**, 104101 (2023).
- [37] P. Pathak, V. K. Yadav, S. Das, and D. Mallick, in *2023 IEEE 36th International Conference on Micro Electro Mechanical Systems (MEMS)* (IEEE, Munich, Germany, 2023), p. 1033.
- [38] Z. Zhang, L. Zhou, P. E. Wigen, and K. Ounadjela, Using ferromagnetic resonance as a sensitive method to study temperature dependence of interlayer exchange coupling, *Phys. Rev. Lett.* **73**, 336 (1994).
- [39] M. Farle, Ferromagnetic resonance of ultrathin metallic layers, *Rep. Prog. Phys.* **61**, 755 (1998).
- [40] Y.-L. Zhao, Q.-P. Chen, Y.-G. Zhao, L. Pan, and Y. Sun, Time-dependent magnetoelectric effect in Fe/Pb(Mg<sub>1/3</sub>Nb<sub>2/3</sub>)<sub>0.7</sub>Ti<sub>0.3</sub>O<sub>3</sub> heterostructure: A ferromagnetic resonance study, *Appl. Phys. Lett.* **103**, 082905 (2013).
- [41] T. Nan, Z. Zhou, M. Liu, X. Yang, Y. Gao, B. A. Assaf, H. Lin, S. Velu, X. Wang, and H. Luo, *et al.*, Quantification of strain and charge co-mediated magnetoelectric coupling on ultra-thin permalloy/PMN-PT interface, *Sci. Rep.* **4**, 1 (2014).
- [42] X. Tong, K. Lin, D. Lv, M. Yang, Z. Liu, and D. Zhang, Optical properties of PMN-PT thin films prepared using pulsed laser deposition, *Appl. Surf. Sci.* **255**, 7995 (2009).
- [43] K. C. Kao, *Dielectric Phenomena in Solids* (Elsevier, 2004), <https://shop.elsevier.com/books/dielectric-phenomena-in-solids/kao/978-0-12-396561-5>.
- [44] T. Yoshino, K. Ando, K. Harii, H. Nakayama, Y. Kajiwara, and E. Saitoh, Universality of the spin pumping in metallic bilayer films, *Appl. Phys. Lett.* **98**, 132503 (2011).
- [45] E. Della Torre, L. H. Bennett, and R. E. Watson, Extension of the Bloch  $T^{3/2}$  law to magnetic nanostructures: Bose-Einstein condensation, *Phys. Rev. Lett.* **94**, 147210 (2005).
- [46] D. Zhang, K. Klabunde, C. Sorensen, and G. Hadjipanayis, Magnetization temperature dependence in iron nanoparticles, *Phys. Rev. B* **58**, 14167 (1998).

- [47] M. D. De Sihues, P. Silva, and J. Fermin, Effect of temperature on the ferromagnetic resonance of  $\text{Ni}_{50}\text{Fe}_{50}$  thin films, *Phys. B: Condens. Matter* **354**, 361 (2004).
- [48] B. K. Kuanr, V. Veerakumar, A. V. Kuanr, R. Camley, and Z. Celinski, Effect of temperature on the ferromagnetic-resonance field and line width of epitaxial Fe thin films, *IEEE Trans. Magn.* **45**, 4015 (2009).
- [49] S. Choi, T. R. ShROUT, S. Jang, and A. Bhalla, Morphotropic phase boundary in  $\text{Pb}(\text{Mg}_{13}\text{Nb}_{23})\text{O}_3\text{-PbTiO}_3$  system, *Mater. Lett.* **8**, 253 (1989).
- [50] A. Azevedo, R. O. Cunha, F. Estrada, O. Alves Santos, J. B. S. Mendes, L. H. Vilela-Leão, R. L. Rodríguez-Suárez, and S. M. Rezende, Electrical detection of ferromagnetic resonance in single layers of permalloy: Evidence of magnonic charge pumping, *Phys. Rev. B* **92**, 024402 (2015).